Acta Astronautica 238 (2026) 1432–1446

Contents lists available at ScienceDirect

Acta Astronautica

journal homepage: www.elsevier.com/locate/actaastro

Research paper

# Monitoring Cislunar fragmentation events using a constellation of space-based observers ☆

C. Gambarotto, P. Grattagliano *, L. De Maria, M.F. Montaruli

*Department of Aerospace Science and Technology, Politecnico di Milano, Via G. La Masa, 34, Milan, 20156, Italy*

ARTICLE INFO

*Keywords:*
Cislunar space
Fragmentation events
Space debris
Space Surveillance and Tracking
Space-based observations

ABSTRACT

The increasing number of Cislunar missions in recent decades, driven by Moon's economic, scientific, military, and commercial potential, has increased concerns about collision threats, and the widespread proliferation of debris. To safeguard future missions and infrastructure, a robust Space Traffic Management system is essential. However, current sensor capabilities are insufficient for large-scale Cislunar Space Situational Awareness, leaving a critical observational gap in this appealing region. Currently, a constellation of space-based passive optical sensors, strategically positioned to cover key areas, remains the only viable solution. While previous studies explored the observational capabilities of various Cislunar orbits for tracking individual objects on specific trajectories, none systematically analyzed their effectiveness in monitoring debris clouds generated by collision events. This study addresses this gap by assessing the observational potential of key Cislunar and lunar orbital families in tracking debris clouds over time, offering critical insights for the sustainable planning of future Cislunar operations.

Twenty-nine orbits from distinct orbital families are selected to host the observers, based on their stability and SSA relevance, and eleven catastrophic collision events, spatially distributed across the region, are simulated using the NASA Standard Breakup Model. The resulting debris are propagated within the Circular Restricted Three-Body Problem dynamical framework over a three-month period. The possible impact threats to the Earth, the Moon, and spacecraft in Geostationary Orbit (GEO) are assessed, as well as the observers' performance in tracking the debris.

Results indicate moderate risks to the two celestial bodies but no significant threats to GEO belt assets. The L2 Halo orbit family emerges as the most effective for long-term debris monitoring, achieving the highest performance when integrated into a constellation with small Lyapunov, Distant Retrograde, and Elliptical Lunar Orbits. Notably, the primary factors limiting fragment detectability include the vast spatial extent of the Cislunar region and occasional obstructions by celestial bodies.

## 1. Introduction

Currently, over one hundred missions targeting the Moon and its surroundings are either planned or underway, driven by goals such as exploiting lunar resources, establishing long-term lunar habitats, and constructing deep-space infrastructure like NASA's Gateway [1–3]. An increased orbital traffic is therefore expected, raising concerns about fragmentation events and widespread debris proliferation within the complex and chaotic orbital environment of Cislunar space. As previous studies have warned [4–7], such debris threatens not only lunar missions but also Near-Earth assets. Consequently, effective risk mitigation becomes critical, necessitating precise, real-time tracking of objects through a robust Space Traffic Management (STM) framework.

However, current Earth-based surveillance capabilities remain insufficient for large-scale monitoring of Cislunar space, leaving a significant and dangerous opening [2,8]. Currently, a constellation of strategically positioned passive optical sensors, on optimized Cislunar orbits for Space Situational Awareness (SSA), is the only promising solution.

Furthermore, in Earth-centered orbital regimes, fragmentation is a well-established issue that has been addressed through both scientific research and operational measures, particularly within the framework

☆ This research has received funding as part of the work developed for the agreement n.2023-37HH.0 for the project "Attività tecnico-scientifiche di supporto a C-SSA/ISOC e simulazione di architetture di sensori per SST", established between the Italian Space Agency (ASI) and Politecnico di Milano (POLIMI).

* Corresponding author.
*E-mail addresses:* chiara.gambarotto@mail.polimi.it (C. Gambarotto), paola.grattagliano@polimi.it (P. Grattagliano), luigi.demaria@polimi.it (L. De Maria), marcofelice.montaruli@polimi.it (M.F. Montaruli).

https://doi.org/10.1016/j.actaastro.2025.09.078
Received 7 July 2025; Received in revised form 20 September 2025; Accepted 26 September 2025
Available online 30 September 2025
0094-5765/

of Space Surveillance and Tracking (SST) services [9–17]. These efforts underline the importance of a deeper understanding of how fragments are generated and evolve, even in the vast Cislunar environment. Such knowledge is essential for developing more efficient and accurate tracking models, with increasing implications for the operational management of space assets and the long-term sustainability of space activities.

Although prior studies have investigated the observability of individual targets within Cislunar orbital families [8,18–28], a critical gap remains in correlating fragmentation events and debris propagation to observational capabilities.

This study contributes to closing this gap by evaluating the observational potential of key orbital families in detecting debris generated by eleven catastrophic Cislunar collisions, as well as assessing the threat posed to celestial bodies and active assets in Geostationary Earth Orbits (GEO).

A total of twenty-nine observer orbits from a range of Cislunar periodic families within the Circular Restricted Three-Body Problem (CR3BP) and lunar orbits, are selected. These orbits were chosen based on criteria such as dynamical stability, scientific value, SSA relevance, and their capacity to provide comprehensive regional coverage [2,3,7,22,29–36]. The capability of these observer orbits to detect the evolution of debris within CR3BP dynamics over a three-month period is evaluated, both individually and within constellation configurations of up to ten collaborative observers.

The structure of this paper is organized as follows. Section 2 outlines the methodology employed for characterizing fragmentation, propagating debris and assessing observability. Section 3 describes the development of the test case, including the foundational assumptions, design considerations, and selection criteria. Section 4 presents a detailed analysis of the simulation results.

## 2. Methodology

This section presents an overview of the key metrics employed in this study, with particular emphasis on the mathematical models used to simulate fragmentation events (Section 2.1), propagate debris trajectories (Section 2.2), and model sensor detections (Section 2.3), thereby enabling the evaluation of space object observability over time.

### 2.1. Collision events model

The NASA Standard breakup Model (SBM), implemented in EVOLVE 4.0 and developed by Johnson and Krisko [37], is a stochastic model grounded in empirical data derived from space surveillance catalogues and ground-based experiments dating back to the early 1980s. The SBM characterizes debris clouds generated by fragmentation events by providing statistical distributions for fragment mass, velocity, area-to-mass ratio, and characteristic length.

The model simulates two distinct types of fragmentation events: collisions and explosions. Collisions are further categorized as either catastrophic or non-catastrophic based on the impact energy per unit target mass. A threshold of 40 J/g is used to distinguish between these categories, with collisions falling below this threshold classified as non-catastrophic. For collision scenarios, the fragment assignment to parent bodies follows the methodology proposed by Schuhmacher [38]. Initially, fragments exceeding the size of the projectile are attributed to the target. Subsequently, for the remaining fragments, assignment is determined by considering the relative masses of the parent bodies, normalized to the total fragment mass output of the simulation.

Following the fragment assignment, the final velocity of each fragment is computed by summing the velocity of the respective parent body with the delta-V derived from the SBM statistical distribution. Instead, the fragment position vector is set equal to that of the parent at the instant of the breakup.

### 2.2. Circular Restricted three body problem

Cislunar space is defined as the region influenced by the gravitational forces of both the Earth and the Moon [2]. The most suitable and simple dynamical model for describing the motion of a spacecraft or fragment within this region, subject to these gravitational forces, is the CR3BP. In this formulation, the two primary bodies, denoted as $P_1$ (Earth) and $P_2$ (Moon), follow circular, coplanar orbits around their common center of mass, while a third body, $P_3$ (spacecraft or fragment), assumed to have negligible mass, moves under their combined gravitational influence.

The CR3BP employs a rotating, non-dimensional Synodic reference frame centered at the system barycenter. Within this frame, the primary bodies remain stationary along the x-axis, allowing the derivation of the equations of motion for the third body $P_3$:

$$\ddot{x} - 2\dot{y} = \frac{\delta U}{\delta x} \qquad \ddot{y} + 2\dot{x} = \frac{\delta U}{\delta y} \qquad \ddot{z} = \frac{\delta U}{\delta z} \tag{1}$$

where $U$ is the potential function expressed by:

$$U = \frac{1}{2}(x^2 + y^2) + \frac{1-\mu}{r_1} + \frac{\mu}{r_2} \tag{2}$$

Here, $r_1$ and $r_2$ represent the distances between the third body ($P_3$) and the two primary bodies ($P_1$ and $P_2$) respectively:

$$r_1 = [(x + \mu)^2 + y^2 + z^2]^{\frac{1}{2}} \tag{3}$$

$$r_2 = [(x - 1 + \mu)^2 + y^2 + z^2]^{\frac{1}{2}} \tag{4}$$

The parameter $\mu = m_2/(m_1 + m_2)$ represents the system mass parameter. For the Earth-Moon system, $\mu$ is approximately 0.01215.

The CR3BP constitutes a conservative, time-invariant dynamical system that admits only one integral of motion, the Jacobi Constant (JC):

$$JC = 2U - v^2 = 2U - \dot{x}^2 - \dot{y}^2 - \dot{z}^2 \tag{5}$$

where $U$ represents the potential energy, and $v$ is the velocity of the third body, expressed as the norm. This key parameter plays a pivotal role in classifying admissible orbits within the CR3BP.

Within the Synodic reference frame, five equilibrium points, known as Lagrange Points, exist. Around these points, a variety of relevant periodic closed orbits, repeating over a constant period and grouped into families, can be found [29]. Particular focus is posed on the more stable ones, as they require lower station-keeping efforts and reduce long-term mission costs. The stability of periodic orbits is evaluated using a Stability Index $\nu$, defined from the Monodromy Matrix (MM) [29]. The MM corresponds to the State Transition Matrix $\Phi$, evaluated over one complete orbital period, with the Stability Index defined as:

$$\nu_1 = \frac{1}{2}(|\lambda_{max}| + |\frac{1}{\lambda_{max}}|), \quad \nu_1 \geq 1 \tag{6}$$

where $\lambda_{max}$ is the Monodromy Matrix eigenvalue of maximum modulus. Orbits with a stability index of 1 are considered stable, whereas those with significantly larger indices exhibit increasing instability.

Within these families, certain orbits are particularly well-suited for scientific missions and SSA applications [1,29,39,40]. Of particular interest are the stable three-dimensional Halo orbits [4,7,35] and Near-Rectilinear Halo Orbits (NRHOs), which have garnered significant attention due to their favorable dynamical stability and accessibility to the Moon. Notably, an $L_2$ NRHO has been selected for both the CAPSTONE mission [41] and the planned Lunar Orbital Platform-Gateway [3]. Equally important are the Distant Retrograde Orbits (DROs), which offer long-term dynamical stability and have been employed in various mission profiles, including Artemis I and China's Chang'e 5 mission

[35,36]. In addition, two-dimensional periodic Lyapunov orbits associated with the Earth-Moon $L_1$ and $L_2$ Lagrange points [2,8,22], as well as short-period orbits around $L_4$ and $L_5$ [2,7,8], are noteworthy. These orbits, which revolve around their respective Lagrange points, are of particular interest for observational platforms aimed at monitoring these dynamically significant and often underexplored regions of Cislunar space.

### 2.3. Observability and detectability model

The methodology described in [22] is used to assess the capability of space-based optical sensors to detect a target, specifically the fragments in this study, within the Cislunar region. A target is considered visible from a space-based sensor if its apparent visual magnitude is less than 20, and if the angular separation between the observer-target vector and the target-celestial body vector exceeds the following thresholds: 50° for the Sun, 35° for the Earth, and 30° for the Moon. These criteria ensure that the target remains within an optimally illuminated and unobstructed field of view.

The apparent magnitude of the space object is determined using the following equation:

$$mag_{sc} = mag_{sun} - 2.5 \log_{10} \frac{I_{sc}}{I_{sun}} \tag{7}$$

where $mag_{sun}$ represents the Sun apparent reference magnitude, $I_{sc}$ is the irradiance of the spacecraft, and $I_{sun}$ is the reference irradiance of the Sun. Both the target fragments and the observing spacecraft are modeled as Lambertian spheres with a reflection coefficient of 0.5 [22]. The lower the magnitude, the greater is the capacity of an observer to detect the target fragment. The irradiance reflected by the target is given by:

$$I_{sc} = \frac{I_{sun}}{\|\mathbf{r}_{\mathbf{sc-obs}}\|^2} \frac{2}{3} \frac{C_d}{\pi^2} r^2 (\sin\alpha + (\pi - \alpha)\cos\alpha) \tag{8}$$

where $r$ represents the fragment characteristic dimension, $C_d$ is the diffuse reflection coefficient, $\alpha$ is the phase angle between the Sun and the observer as viewed from the target and $\mathbf{r}_{\mathbf{sc-obs}}$ denotes the distance vector between the target and the observer, expressed in the J2000 reference frame.

## 3. Test cases design

To evaluate the capability of space-based optical sensors to detect fragments within the Cislunar region, it is necessary to identify and select relevant orbits. Key locations for current and future missions include the periodic families within the CR3BP, regarded to be at higher risk for potential catastrophic fragmentation events [1–4,7,33,35,36]. Moreover, these orbits, owing to their periodicity, low station-keeping costs, and extensive coverage of the Cislunar region, further represent the most promising candidates for the establishment of a Cislunar SSA constellation [1,2,4,7,8,18,21,22,33].

Thus, nine families of periodic orbits are selected for potential Cislunar observation: DRO, L4 Planar, L5 Planar, L1 Lyapunov, L1 Northern Halo, L1 Southern Halo, L2 Lyapunov, L2 Northern Halo, and L2 Southern Halo.

Although several of these orbits (specifically, the L2 Halo and NRHO [4,6], the DRO [4], and the L2 Lyapunov orbit [5]) have previously been examined in explosion-cases studies, due to their particular significance for upcoming scientific and SSA missions, they are also considered in this study. This choice allows a focused examination of the differences in outcomes associated with distinct types of fragmentation events, hence contributing to and extending the existing body of literature.

A total of eleven collision scenarios are simulated across ten orbits within these families. A single collision is simulated for each family, with the exception of the Halos, which include an additional collision on the LUMIO's orbit [42]. Moreover, an additional simulation is

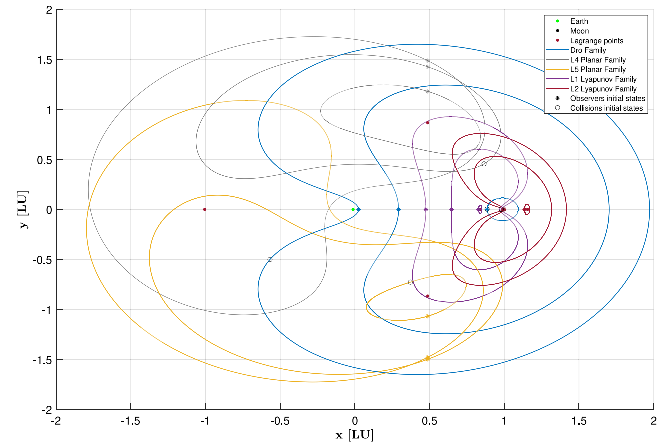


**Fig. 1.** Collisions locations (empty circles) and observers initial positions (asterisks) on planar orbits in Synodic reference frame — Plane x–y view.

opportunely performed on the larger DRO, which presents the closest Earth approach among the orbits considered in this study, to further investigate the potential threats associated with near-Earth fragmentation events. To characterize the collisions, the NASA SBM model is employed, validated, and used to model the resulting debris [5].

For computational efficiency, all collisions are treated as catastrophic events [37]. To ensure consistency when comparing final results, collisions between the two same spacecraft (with masses respectively of 550 kg and 682 kg), occurring on the 1 January 2000 at 12:00:00.000 UTC, are replicated over eleven different locations, varying only the impact velocity of the two colliding bodies. This approach is supported by the findings of Black and Frueh [5], which emphasize the significant influence of the parent's orbit and initial state on the evolution of debris fragments. Therefore, selecting a consistent collision scenario across varying orbital environments allows for an isolated assessment of the influence of orbital location and kinematics on fragmentation outcomes.

Each catastrophic collision generates 1074 fragments. This number is directly retrieved from the SBM [37]: $N(L_c) = 0.1 \cdot (m_1 + m_2)^{0.75} \cdot L_c^{-1.71}$. $N(L_c)$ denotes the number of fragments with a characteristic length greater than $L_c$, and $m_1$ and $m_2$ represent the masses of the two colliding bodies. The minimum fragment size considered $L_c$ in this model is set to 10 cm, in accordance with Johnson recommendation [37], as the model has been validated only for particles exceeding this threshold. The fragments are then propagated in the CR3BP for three months. Given the large scale of the simulations and the study focus on a broad characterization of debris behavior, this dynamical model was selected in spite of higher-fidelity ones for its computational efficiency and ability to provide a sufficiently accurate approximation over the timespan considered. The resulting debris are then filtered by discarding fragments with unrealistically high velocities, avoiding non-physical behaviors from the analysis. Indeed, due to its simplified assumptions about energy distribution, fragmentation mechanics, material properties, and object strength, the model may overestimate fragment velocities, requiring a further control.

For each collision scenario, the parents states and impact velocities are reported in Table 1. The collision sites, appropriately distributed across the entire region, are illustrated in the Earth–Moon Synodic reference frame in Figs. 1 and 2 (in the x–y plane), in Fig. 3 (in the x–z plane) and in Fig. 4 (in three dimensions).

For each of the nine families selected, three space-based observers are considered, prioritizing the most stable orbits while ensuring a range of orbital periods. This approach facilitates the development of a comprehensive observational constellation able to cross vast regions of Cislunar space and maintain targeted coverage of key locations, such

**Table 1**
Adimensional target and projectile states with corresponding impact velocity at collision, expressed in the Earth-Moon Synodic reference frame.

| Collision ID | Orbital family | Position at collision | | | Velocity at collision | | | Impact velocity [LU/TU] |
|---|---|---|---|---|---|---|---|---|
| | | x [LU] | y [LU] | z [LU] | $v_x$ [LU/TU] | $v_y$ [LU/TU] | $v_z$ [LU/TU] | |
| 1 | DRO | 0.8848 | 0.0028 | 0 | 0.0100<br>−0.0951 | 0.4704<br>0.3648 | 0<br>−0.3934 | 0.4705 |
| 2 | DRO | −0.5683 | −0.5006 | 0 | 0.6601<br>0.3686 | 1.1190<br>0.8275 | 0<br>−1.0860 | 1.2992 |
| 3 | L4 Planar | 0.8644 | 0.4553 | 0 | −0.4234<br>−0.5486 | −0.3637<br>−0.4890 | 0<br>−0.4667 | 0.5582 |
| 4 | L5 Planar | 0.3718 | −0.7268 | 0 | 0.3316<br>0.2495 | 0.1543<br>0.0722 | 0<br>−0.3058 | 0.3657 |
| 5 | L1 Lyapunov | 0.9792 | 0.0013 | 0 | −0.1152<br>−0.4993 | −1.7080<br>−2.0921 | 0<br>−1.4314 | 1.7119 |
| 6 | L1 N Halo | 0.9897 | 0 | −0.0417 | 0<br>−0.1634 | −0.7303<br>−0.8941 | −0.0015<br>−0.6121 | 0.7303 |
| 7 | L1 S Halo | 0.9290 | 0.1066 | −0.1018 | 0.1497<br>0.0775 | 0.0441<br>−0.0280 | 0.2812<br>0.0123 | 0.3216 |
| 8 | L2 Lyapunov | 1.4159 | 0 | 0 | 0<br>−0.1665 | −0.7441<br>−0.9110 | 0<br>−0.6222 | 0.7441 |
| 9 | L2 N Halo | 0.9895 | −0.0032 | 0.1004 | −0.0047<br>−0.1003 | −0.0131<br>−0.1087 | −0.2126<br>−0.5687 | 0.4260 |
| 10 | L2 S Halo | 0.9881 | −0.0119 | −0.0032 | −0.0729<br>−0.3791 | 0.8007<br>0.4945 | 1.1026<br>−0.0384 | 1.3646 |
| 11 | L2 S Halo | 1.0690 | 0.0245 | 0.0689 | 0.0066<br>−0.0641 | 0.3100<br>0.2393 | −0.0565<br>−0.3201 | 0.3152 |

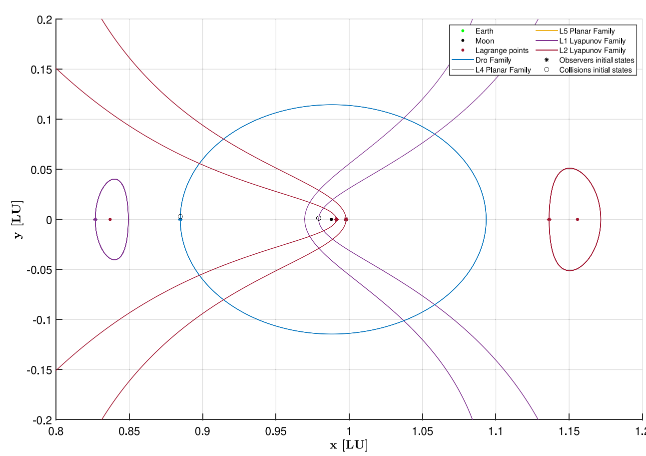


**Fig. 2.** Collisions locations (empty circles) and observers initial positions (asterisks) on planar orbits in Synodic reference frame — Plane x–y view. Zoom in x ∈ [-0.8 LU, 1.2 LU], y ∈ [-0.2 LU, 0.2 LU].

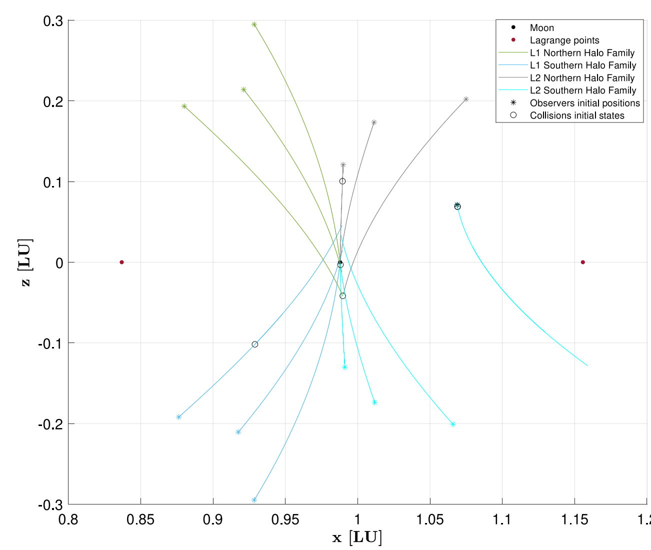


**Fig. 3.** Collisions locations (empty circles) and observers initial positions (asterisks) on Halo orbits in Synodic reference frame — Plane x–z view.

as the Lagrange points and the lunar surface. An exception is made for the L2 South Halo family, for which four observers are considered instead of three, including the candidate trajectories for the LUMIO mission (observer 28) and the Gateway station (observer 25) [3,42]. Of relevance is also observer 3, positioned on a DRO candidate for the future ESA LUMOS (LUnar MOnitoring System) mission [30,43].

In total, twenty-eight observers are selected, illustrated in Fig. 4. For each observer, the initial state vector in the Synodic reference frame is provided in Table 2, along with the corresponding orbital period.

An additional observer in an Elliptical Lunar Orbit (ELO) is incorporated to evaluate the capability of a space-based observer orbiting the Moon. Given that approximately 25% of planned lunar missions intend to deploy orbiters for scientific research, monitoring, communications, and surveillance purposes [1], the inclusion of such an observer is both relevant and justified. For this study, a frozen, high-altitude elliptical orbit is selected due to its inherent stability and minimal station-keeping requirements. This orbit configuration enables continuous coverage of the lunar poles while facilitating extensive monitoring of the broader Cislunar region [31]. The initial conditions of the ELO, expressed in the Moon-fixed International Astronomical Union (IAU) reference frame [44], are provided in Table 3.

To ensure the validity of the visibility assessment (Section 2.3) and to maintain an adequate line of sight, the initial positions of the observers are offset from the collision locations, as depicted in Figs. 1, 3 and 4.

The celestial bodies positions are retrieved from the SPICE Ephemerides (JPLDE425s) [44] in the J2000 reference frame, for each epoch $t$ of the time window considered. For the same instants, the positions of observers and fragments are transformed from the time-independent Synodic reference frame to the time-dependent J2000 frame using the method outlined in Appendix. Once the position vectors

**Table 2**
Observers adimensional initial states and periods, expressed in the Earth-Moon Synodic reference frame. For each of the nine orbital families selected, three orbits are chosen to host the observers. Only for the L2 South Halo family, four orbits are considered, including the candidate trajectories for the LUMIO mission (observer 28) and the Gateway station (observer 25) [3,42]. Of relevance is also observer 3, positioned on a DRO candidate for the future ESA LUMOS mission [30,43].

| Observer ID | Observer family | $x_0$ [LU] | $y_0$ [LU] | $z_0$ [LU] | $v_{x0}$ [LU/TU] | $v_{y0}$ [LU/TU] | $v_{z0}$ [LU/TU] | Period [TU] |
|---|---|---|---|---|---|---|---|---|
| 1 | DRO | 0.024 | −1.923e−26 | −5.033e−32 | 1.068e−12 | 7.223 | −6.005e−30 | 6.305 |
| 2 | DRO | 0.292 | −4.277e−23 | 1.136e−22 | 2.512e−12 | 2.046 | −3.000e−22 | 6.228 |
| 3 | DRO | 0.884 | −1.764e−27 | 9.291e−36 | −3.462e−15 | 0.470 | 6.285e−35 | 1.579 |
| 4 | L4 Planar | 0.487 | 1.425 | 6.797e−34 | 8.439e−01 | −0.432 | −4.216e−34 | 6.425 |
| 5 | L4 Planar | 0.487 | 1.180 | 8.982e−24 | 4.730e−01 | −0.216 | −9.841e−25 | 6.533 |
| 6 | L4 Planar | 0.487 | 1.486 | −1.838e−22 | 1.039e+00 | −0.766 | 5.529e−23 | 6.290 |
| 7 | L5 Planar | 0.487 | −1.067 | 2.047e−24 | −3.066e−01 | −0.134 | −2.337e−24 | 6.562 |
| 8 | L5 Planar | 0.487 | −1.497 | 1.243e−35 | −9.714e−01 | −0.537 | 2.321e−34 | 6.371 |
| 9 | L5 Planar | 0.487 | −1.478 | −2.166e−24 | −1.031e+00 | −0.779 | −3.030e−25 | 6.287 |
| 10 | L1 Lyapunov | 0.647 | −3.250e−23 | −2.652e−26 | 3.048e−13 | 0.759 | −7.297e−25 | 6.529 |
| 11 | L1 Lyapunov | 0.475 | 1.218e−22 | −1.853e−26 | −3.528e−13 | 1.235 | −2.397e−25 | 7.381 |
| 12 | L1 Lyapunov | 0.826 | 6.437e−29 | 4.958e−32 | 1.011e−15 | 0.091 | −2.040e−32 | 2.7179 |
| 13 | L1 N Halo | 0.921 | −1.181e−27 | 2.140e−01 | 1.125e−13 | 0.132 | −6.561e−13 | 1.804 |
| 14 | L1 N Halo | 0.880 | −9.811e−27 | 1.933e−01 | −5.203e−14 | 0.223 | 1.652e−13 | 2.126 |
| 15 | L1 N Halo | 0.928 | 1.173e−25 | 2.948e−01 | 8.979e−11 | 0.082 | −4.195e−10 | 2.167 |
| 16 | L1 S Halo | 0.876 | 5.114e−27 | −1.919e−01 | −4.990e−14 | 0.2301 | −1.480e−13 | 2.172 |
| 17 | L1 S Halo | 0.928 | 1.173e−25 | −2.948e−01 | 8.979e−11 | 0.082 | 4.195e−10 | 2.1675 |
| 18 | L1 S Halo | 0.917 | −1.497e−27 | −2.105e−01 | −8.364e−14 | 0.142 | −3.816e−13 | 1.812 |
| 19 | L2 Lyapunov | 0.991 | 2.943e−29 | −7.127e−92 | 4.236e−14 | 2.655 | −1.887e−88 | 7.813 |
| 20 | L2 Lyapunov | 1.136 | −1.127e−28 | −2.848e−33 | 6.974e−16 | 0.099 | 1.178e−33 | 3.386 |
| 21 | L2 Lyapunov | 0.997 | 2.331e−27 | −2.739e−36 | −8.270e−14 | 1.567 | 4.197e−33 | 6.518 |
| 22 | L2 N Halo | 1.011 | −3.465e−28 | 1.734e−01 | −6.888e−13 | −0.078 | 1.011e−11 | 1.3673 |
| 23 | L2 N Halo | 0.024 | −1.923e−26 | −5.033e−32 | 1.068e−12 | 7.223 | −6.005e−30 | 6.305 |
| 24 | L2 N Halo | 0.292 | −4.277e−23 | 1.136e−22 | 2.512e−12 | 2.046 | −3.000e−22 | 6.228 |
| 25 | L2 S Halo | 0.884 | −1.764e−27 | 9.291e−36 | −3.462e−15 | 0.470 | 6.285e−35 | 1.579 |
| 26 | L2 S Halo | 0.487 | 1.425 | 6.797e−34 | 8.439e−01 | −0.432 | −4.216e−34 | 6.425 |
| 27 | L2 S Halo | 0.487 | 1.180 | 8.982e−24 | 4.730e−01 | −0.216 | −9.841e−25 | 6.533 |
| 28 | L2 S Halo | 1.068 | 0 | 0.071 | 0 | 0.319 | 0 | 3.259 |

**Table 3**
ELO's observer 29 initial state in Moon-fixed IAU reference frame.

| x [km] | y [km] | z [km] | $v_x$ [km/s] | $v_y$ [km/s] | $v_z$ [km/s] |
|---|---|---|---|---|---|
| −4486.1 | 3003.2 | 3693.3.3 | −0.4816 | −0.7194 | 0 |

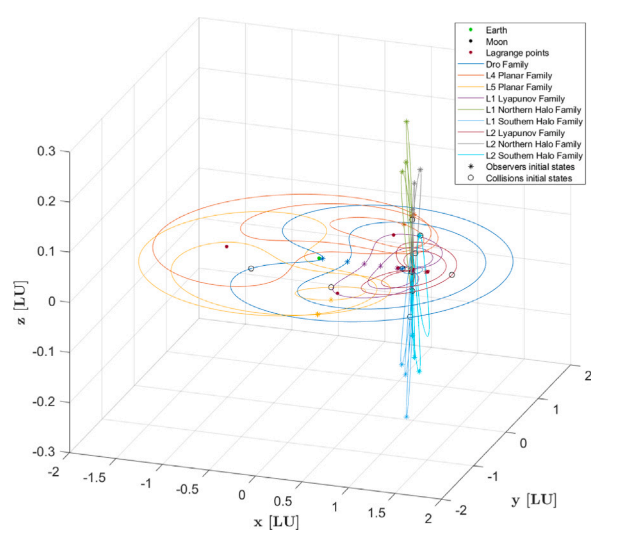


**Fig. 4.** Observer orbits illustrated in the Earth-Moon Synodic reference frame — 3D View.

are known in the J2000 frame, the required phase and exclusion angles are computed following the steps presented in Section 2.3 and setting the diffuse reflection coefficient $C_d$ to 0.5. For the ELO observer, the transformation of coordinates required for the visibility analysis (Section 2.3) from the *IAU_Moon* reference frame to J2000 is executed using SPICE built-in function *cspice_spkez* [44] at each analyzed time step. Furthermore, as the ELO remains within the Moon Sphere of Influence (SOI), its trajectory is computed using a two-body dynamical model.

## 4. Results

This section presents the results of the study. It begins with a risk assessment analysis (Section 4.1) aimed at evaluating the potential hazards posed by Cislunar-generated debris to the Earth, the Moon, and operational spacecraft in GEO over time. This is followed by an evaluation of the observers observational performance, focusing on their effectiveness in monitoring the debris clouds (Section 4.2). Finally, an analysis is conducted to investigate how the monitoring performance is affected when multiple observers operate collaboratively (Section 4.3).

It is important to note that these findings are specific to the selected propagation period and initial epoch. Consequently, these results should not be generalized as universally applicable, since factors such as solar activity and other dynamical influences may vary with different collision epochs.

### 4.1. Debris propagation and risk assessment

The initial phase of this study is dedicated to the analysis of potential threats posed by fragments resulting from a breakup to both celestial bodies and assets in GEO. This orbital region is of particular concern due to its high density of operational satellites, making it one of the most hazardous areas. In this analysis, an impact or entry event is considered when the norm of the relative distance between the position vectors of the fragment and the celestial bodies is less than or equal to the radius of the celestial body considered. A threat to the GEO region

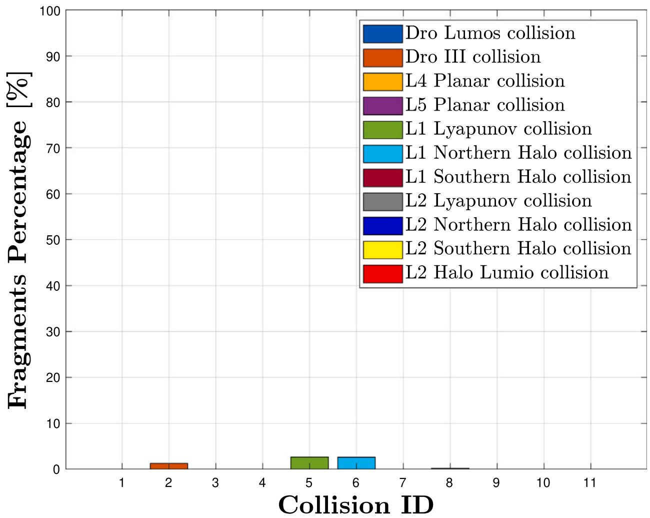


**Fig. 5.** Percentage of fragments, generated from each collision, impacting the Earth surface, over a three-month propagation period. The impact is registered when norm of the relative distance between the position vectors of the fragment and the Earth is less than or equal to the Earth radius.

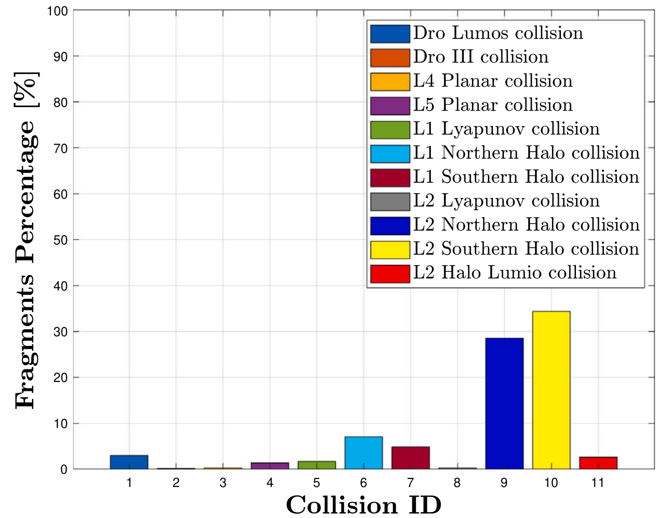


**Fig. 6.** Percentage of fragments, generated from each collision, impacting the Moon surface, over a three-month propagation period. The impact is registered when norm of the relative distance between the position vectors of the fragment and the Moon is less than or equal to the Moon radius.

instead is considered to occur when the relative distance between the fragment and the Earth is lower than the radius of GEO region, as detailed below.

The GEO environment is defined as a region bounded by a circular cross-section, on the x–y plane of the J2000 reference frame, of radius 42,164 km and a tolerance of 10 km along the z-axis.

The percentage of fragments impacting the Earth, the Moon, or entering the GEO region over the three-month period is computed to quantify the threats posed by each collision.

As illustrated in Fig. 5, collisions 5 and 6, occurring in the L1 Lyapunov and L1 Northern Halo orbits respectively, present the highest risks for Earth impacts, with 2.7% and 2.6% of fragments impacting the surface. Interestingly, despite collision 2 occurring closest to Earth, only 1.3% of fragments strike the planet, typically within one to ten days following the collision. No clear correlation is observed between the velocity magnitude of the fragments and the likelihood of impact; rather, the specific direction each fragment takes following the collision appears to be the determining factor. This trend holds true for both the Moon and the GEO region cases. While all impacts from collision 5 occur within one month, impacts from collision 6 continue throughout the three-month period, with the majority occurring around ten to forty days after the event. This is consistent with the dynamics of the CR3BP, where fragments initially evading capture revolve around the system origin before returning into the Earth-Moon environments.

In terms of lunar impact risks, as shown in Fig. 6, the threats are higher, with 34.3% and 28.5% of fragments from the closer collisions 10 and 9, occurring in the Southern and Northern L2 Halo orbits, respectively. These findings are consistent with the results in [4], which identified the highest number of lunar impacts following an explosion in the Southern L2 NRHO.

Smaller risks are associated with collision 6 (7.1%), collision 7 (4.8%), collision 1 on LUMOS DRO (2.9%) and collision 11, on the LUMIO L2 Halo. Notably, collision 11 results in only 2.6% of fragments impacting the Moon, as the majority of fragments disperse rapidly throughout the Cislunar region, away from the lunar surface, under the CR3BP dynamics. This represents a relevant hazard as, unlike Earth, the Moon lacks a substantial atmosphere capable of shielding from incoming objects through aerodynamic heating during re-entry. Therefore, deorbited spacecraft or other orbital debris may impact the lunar surface largely intact, presenting a significant hazard to future lunar infrastructure and human presence.

Regarding the risk to operational spacecraft in GEO, only 0.7% of fragments from collision 2 and 0.3% from collision 6 are registered. It should be noted that the percentages are sufficiently low that a graphical representation would offer no meaningful benefit and therefore not provided. This outcome may appear counterintuitive when compared to the larger number of predicted impacts on Earth, especially considering that the GEO impact criterion is less stringent in terms of relative distance. However, this apparent discrepancy can be explained by the fact that Earth impacts occur even outside the x–y plane in the J2000 reference frame. As such, not all satisfy the planar constraints required for classification as GEO-belt region impacts. In fact, these results suggest that the densely populated GEO belt itself faces relatively low risk, with the majority of hazardous fragments detected along the out-of-plane dimension.

To further explore the evolution and dynamics of the fragments, it is observed that, after three months, the majority of fragments remain dispersed throughout the entire Cislunar region, as highlighted in Fig. 7. In this analysis, this region is defined following the convention in [2], spanning from −1 to 12 Earth radii beyond geostationary orbit (GEO) in the x-direction, and from −9 to 9 GEO in the y-direction, relative to the Earth. In addition to these findings, it is also noteworthy that a significant concentration of fragments is identified over time near the Moon–L1 and Moon–L2 regions, where more stable orbits (Halos and NRHOs) are located. Furthermore, a small portion of fragments originating from collisions 3 and 4, respectively occurring on L4 and L5 planar orbits, tends to accumulate around the more stable region corresponding to the Kordylewski clouds [45].

### 4.2. Observational performance assessment

The objective of this study is to assess the capabilities of Cislunar observational spacecraft in monitoring certain clouds of debris resulting from fragmentation events. To evaluate the detection capability of these monitoring satellites, the visibility of each fragment from each observer is analyzed at each time step, exploiting the methodology presented in Section 2.3. Observations are conducted every two hours over a three-month period. The percentage of fragments successfully observed at least once by each observer-collision pair is presented in Fig. 8. Notably, observers located on the right side of the x-axis, particularly those belonging to the L2 Lyapunov and Halo families, demonstrate

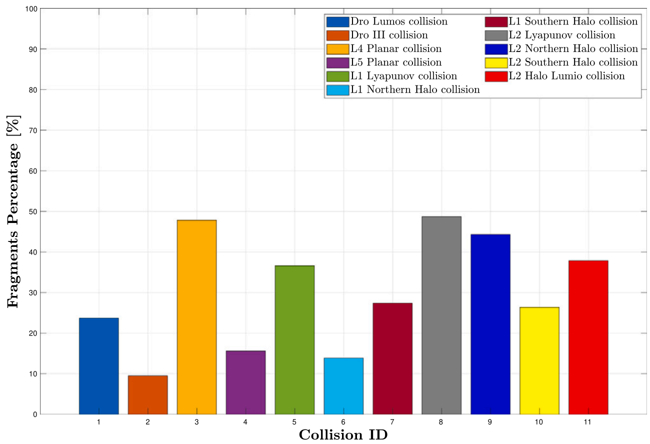


**Fig. 7.** Percentage of fragments, generated from each collision, leaving the Cislunar region boundaries, after a three-month propagation period.

**Table 4**
Violated constraints labels. A fragment is considered visible from an observer if its apparent visual magnitude is less than 20 (MG), and if the angular separation between the observer-fragment vector and the fragment-celestial body vector exceeds the following thresholds: 50° for the Sun (SA), 35° for the Earth (EA), and 30° for the Moon (MA).

| Legend acronym | Violated Constraint (s) | |
|---|---|---|
| MA+EA+SA+MG | Moon Angle+Earth Angle+Sun Angle+Magnitude | |
| EA+SA+MG | Earth Angle+Sun Angle+Magnitude | |
| MA+SA+MG | Moon Angle+Sun Angle+Magnitude | |
| MA+EA+MG | Moon Angle+Earth Angle+Magnitude | |
| MA+EA+SA | Moon Angle+Earth Angle+Sun Angle | |
| SA+MG | Sun Angle+Magnitude | |
| EA+MG | Earth Angle+Magnitude | |
| EA+SA | Earth Angle+Sun Angle | |
| MA+MG | Moon Angle+Magnitude | |
| MA+SA | Moon Angle+Sun Angle | |
| MA+EA | Moon Angle+Earth Angle | |
| MG | Magnitude | |
| SA | Sun Angle | |
| EA | Earth Angle | |
| MA | Moon Angle | |

superior performance across most collision scenarios. Moreover, collision 7, which occurs within the L1 Southern Halo orbit, exhibits the highest overall detection rates, making it the most well-observed event among the analyzed cases. Specifically, collision 7 is detected most effectively by observers 18 (L1 Southern Halo), 26 (L2 Southern Halo), 19 and 21 (L2 Lyapunov), with observer 26 achieving the complete detection of the cloud, while observers 18, 19, and 21 detect 99.3%, 98.8% and 96.7% of fragments, respectively. Observers 3 (DRO), 24 (L2 *N* Halo), 25 (L2 S Halo), and 16 (L1 S Halo) also demonstrate good performance, suggesting their potential role in augmenting constellation observations. The elevated visibility observed in certain collision scenarios can be primarily attributed to the dynamical evolution of observers and fragments following each collision. Specifically, the initial conditions of some collisions result in fragments rapidly drifting away from the observers' orbits and, more broadly, from the Cislunar region, significantly reducing both the duration and probability of detection. Conversely, as will be discussed in greater detail, debris tend to accumulate within more dynamically stable regions, like the ones surrounding the $L_1$ and $L_2$ Lagrange points and the respective stable or quasi-stable orbits such as Lyapunov, Halo, and NRHOs. These zones serve as effective accumulation regions, thereby increasing the likelihood of repeated detection by observers located in proximity.

A limitation of Fig. 8 is the absence of temporal information, which precludes insight into the observers capability to maintain detection of the debris cloud over time. To address this lack, the number of re-observations of each fragment over the three months for the most relevant collision 7 is computed and reported in Fig. 9. Re-observations are defined as instances where a fragment is visible at time step *k* but was not detected at the preceding time step *k-1*. The y-axis in Fig. 9 represents the number of re-observations performed by each observer, while the number of fragments observed that many times is indicated within each box. For instance, observer 1 observes 251 fragments once, 60 fragments twice, and so forth.

Observers 19 and 21 detect a substantial number of fragments but perform relatively few re-observations. In contrast, observers 18, 24, 25, 26, and 3 detect fewer fragments only one time, but much more fragments with higher re-observation rates. Observers capable of sustaining long-term detection, even for a reduced number of fragments, are particularly valuable for constructing and maintaining a comprehensive debris catalogue. Observers 26, 25, and 18 emerge as key candidates for this task, proving Halo orbits especially effective for long-term debris monitoring. Although the ideal scenario involves tracking a large number of fragments over an extended period, this is not always feasible. Therefore, this work prioritizes the observation of fewer fragments with higher accuracy and prolonged durations.

Another key point is to assess how long on the time window considered an observer can contribute to catalogue fragments. To this end, Fig. 10 represents, for each observer, the percentage of fragments originating from collision 7 detected along the three-month time window of the analysis. Most observers detect a large number of fragments in the initial phase, but this number decreases over time, particularly for observers such as 19 and 21, which initially detect many fragments but conduct fewer re-observations. Conversely, observers 18, 26, 25 and 24 maintain consistent observations of a small but still significant fraction of fragments over the three-month period, confirming the findings from the re-observability analysis in Fig. 9.

In fact, a considerable number of fragments drift away within a few days without re-encountering the observers over the time window considered. Observers 18, 26, 25 and 24, on the other hand, exhibit initial detection peaks comparable to other orbits but continue to detect a relevant percentage of fragments thereafter.

To investigate the underlying factors contributing to these trends, the percentage of fragments that remain unobservable due to various constraints is analyzed and presented in Fig. 11, for the observers 18, 19, 24, 25, 26. As each fragment may violate one or more of the constraints outlined in Section 2.3, all these violations are assessed over time. A summary of the acronyms used to denote the different cases of constraint violations is provided in Table 4. The black-stacked lines represent the percentages of visible fragments and are included to provide a complete view of the fragments evolution. As expected, the observed pattern of fragment visibility percentages over time, for each observer, is analogous to the trend shown in Fig. 10.

The primary factor contributing to the non-visibility of fragments within Cislunar space is the increasing distance between the observer and the fragments, which leads to violating the magnitude constraint. This phenomenon is observed across all observers, with a particularly pronounced effect for observer 19 (represented by the orange, salmon, gray, and light green colors). As distance increases, the brightness of the fragments diminishes, leading to higher magnitudes that exceed the detection threshold. Additionally, a smaller, yet significant, fraction of non-visibility arises from periodic occultation by celestial bodies (colors: light blue, salmon and gray for the Moon; red, light pink and gray for the Sun; light green for the Earth). Interestingly, the moon angle constraint has a significant impact during the first half of the observation window, but becomes much less relevant in the second half. In contrast, the constraint imposed by the Sun, while generally less restrictive, remains consistently active throughout the entire period. This behavior can be explained by the initial proximity of the fragments to the Moon: in the early stages, their orbits remain close

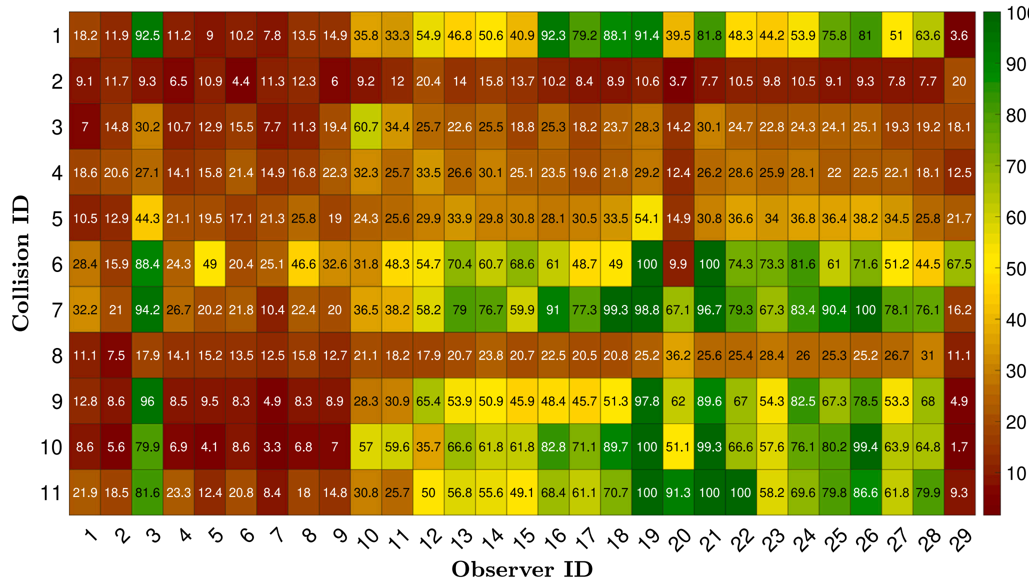


**Fig. 8.** Percentage of fragments generated from each of the eleven collision cases and visible at least once by each observer over three months. Observations are made every two hours.

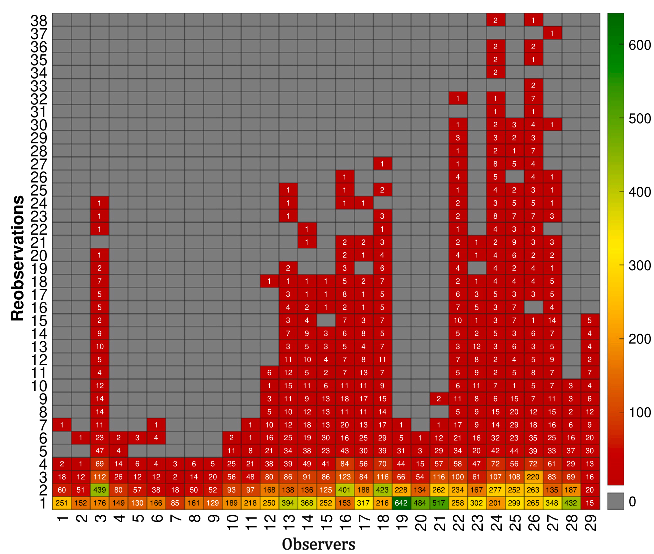


**Fig. 9.** Number of fragment re-observations performed by each observer over three month, for the fragments generated by collision 7. Re-observations are defined as instances where a fragment is visible at time step *k* but was not detected at the preceding time step *k-1*. The y-axis represents the number of re-observations performed by each observer, while the number of fragments observed that many times is indicated within each box. Observations are made every two hours.

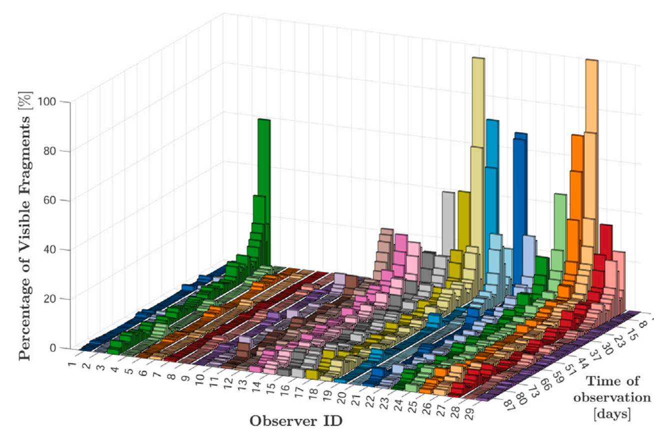


**Fig. 10.** Evolution in time of the percentage of fragments originated by collision 7 and detected by each observer over three months, with time expressed in days.

to the lunar vicinity, making the lunar disk an effective obstruction. As time progresses and the fragments disperse further from the Moon, this constraint naturally loses effectiveness. This trend is particularly evident for observers located on Halo orbits (specifically observers 18, 24, 25, and 26), where the influence of the lunar disk diminishes over time. Notably, observer 19, located on a Lyapunov orbit around the L2 point, exhibits a different behavior: for this configuration, the Moon remains within the critical angular range for the entire observation period, making the constraint continuously relevant. These variations highlight the strong dependence of visibility constraints on the observer orbital configuration, and provide additional insights into the relative impact of celestial obstructions in different dynamical regimes.

Fragments with lower delta velocities (initial $\Delta v$ < 0.4 km/s) are predominantly confined to the inner Cislunar region, allowing for prolonged and more consistent detectability. In contrast, fragments that remain undetected encompass a broad range of initial velocities, spanning both high and low values. The non-detectability of these fragments is primarily influenced by their initial trajectory, which leads to their rapid dispersion across the region and eventual un-observability due to the significant distances involved. Thus, the superior performance of Halo observers can be attributed to their inherent stability, as a significant proportion of fragments, particularly those with lower velocities, persist in the vicinity over time, facilitating prolonged and more consistent detection.

Given the mission relevance, a comparable analysis is performed for collision 11, which occurs along the LUMIO orbit. This assessment also offers insight into the implications of selecting different orbits within the L2 Halo family. As illustrated in Fig. 8, observers 19, 21, and 22 emerge as the most promising, achieving complete detection, with observers 20 (91.3%), 26 (86.6%), and 3 (81.6%) also recording high detection rates.

Upon analyzing re-observations for collision 11 in Fig. 12, a pattern consistent with collision 7 (Fig. 9) is observed: while observers 19,

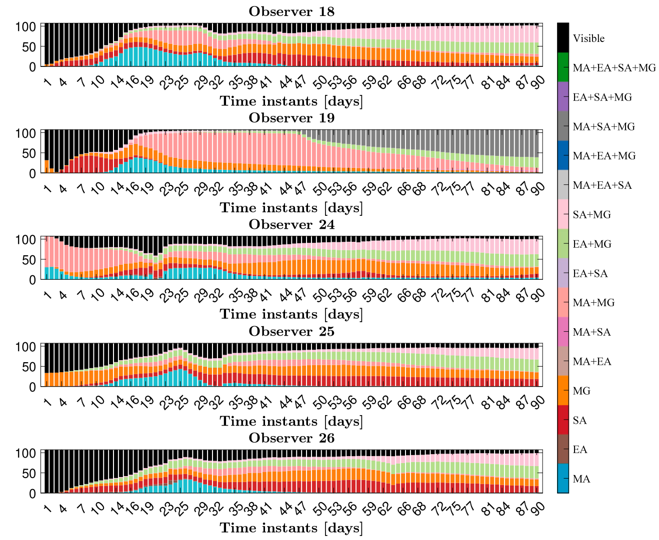


**Fig. 11.** Percentage of collision 7 fragments violating constraints over three months for observers 18, 19, 24, 25, 26. A fragment is considered visible from an observer if its apparent visual magnitude is less than 20 (MG), and if the angular separation between the observer-fragment vector and the fragment-celestial body vector exceeds the following thresholds: 50° for the Sun (SA), 35° for the Earth (EA), and 30° for the Moon (MA). (For interpretation of the references to color in this figure legend, the reader is referred to the web version of this article.)

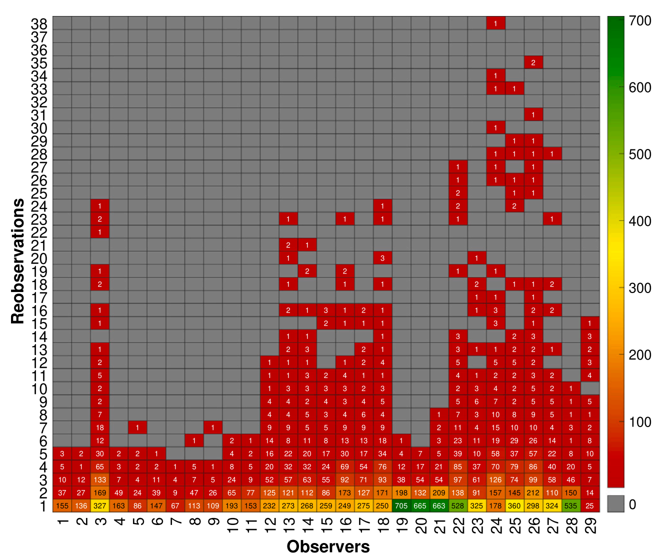


**Fig. 12.** Number of fragment re-observations performed by each observer over three month, for the fragments generated by collision 11. Re-observations are defined as instances where a fragment is visible at time step *k* but was not detected at the preceding time step *k-1*. The y-axis represents the number of re-observations performed by each observer, while the number of fragments observed that many times is indicated within each box. Observations are made every two hours.

20, and 21 detect many fragments, they conduct relatively few re-observations. In contrast, observers 3, 24, and 26, although detecting fewer fragments only one time, achieve higher re-observation rates for a greater number of fragments, further validating L2 Halo orbits and DRO as particularly effective for long-term debris monitoring.

Similarly to Fig. 11, the increasing distances combined with occasional occultation by celestial bodies, result in the majority of fragments becoming non-visible, as highlighted by Fig. 13. Consistent with the earlier analysis, for observers located on Halo orbits, specifically observers 22 and 26, the angular distance constraint imposed by the Moon is particularly significant during the first half of the observation window but becomes considerably less influential in the second half. In contrast, the constraint due to the Sun, though generally less restrictive, remains persistently active throughout the entire time frame. In the case of observers on Lyapunov orbits around L2 (observers 19 and 20), the situation again differs as the constraints imposed by the Sun, the Moon, and even the Earth remain consistently relevant for the entire duration of the observational period. An additional interesting case is presented by the observer located on a DRO (observer 3). For this configuration, the Sun remains a constant constraint, while the influence of the Moon varies more dynamically. Specifically, the lunar constraint becomes significant at the beginning, middle, and end of the window, reflecting the evolving relative geometry between the observer, the fragments, and the Moon as they progress along their respective orbital paths.

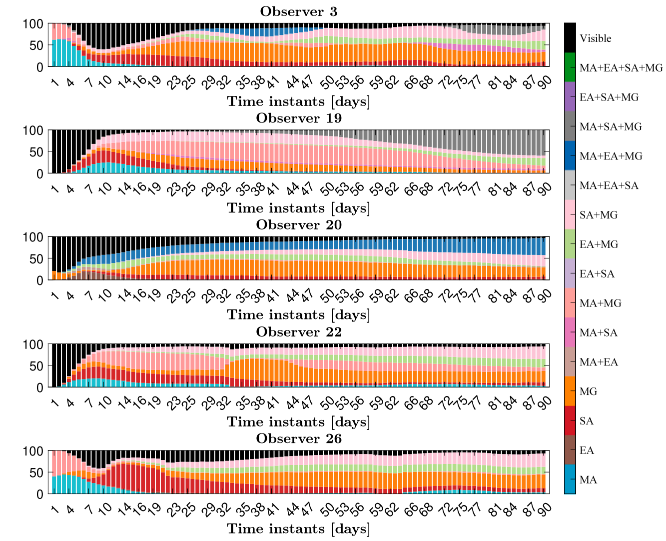


**Fig. 13.** Percentage of fragments generated from collision 11 violating constraints over three months for observers 3, 19, 20, 22, 26. A fragment is considered visible from an observer if its apparent visual magnitude is less than 20 (MG), and if the angular separation between the observer-fragment vector and the fragment-celestial body vector exceeds the following thresholds: 50° for the Sun (SA), 35° for the Earth (EA), and 30° for the Moon (MA).

Since both collision 7 and collision 11 occur on L2 Halo orbits, these similarities are not surprising. Moreover, these findings affirm that while the best-performing observer may vary across different collisions, the L2 Halo family consistently demonstrates superior performance across the analyzed scenarios.

### 4.3. Constellation analysis

The observability analysis presented in the previous section can be extended by investigating how the monitoring performance may be enhanced when multiple spacecraft operate collaboratively within a unified observational constellation. Therefore, a sensitivity analysis is performed by varying the number $n$ of observers in the constellation from two to ten. The candidates for this constellation are the same observers introduced in Section 3, with their initial states detailed in Table 2. The analysis is centered on detecting the debris cloud originating from collision 7, within the L1 Southern Halo orbit. For each specified number $n$ of observers, $\binom{29}{n}$ possible combinations of distinct observers are evaluated. The total visibility time coverage for each fragment is computed and recorded, for every constellation combination. Given

**Table 5**
Occurrences metric: the three top-performing constellation combinations are presented as a function of the number of observers considered. The second column presents the corresponding percentage of fragments for which these combinations provide the longest coverage, while the third column shows the maximum visibility time achieved by each combination. The maximum visibility time is defined as the maximum percentage of time instances within a three-month period during which the combination of observers detects a fragment from collision 7.

| n | Three top-performing observers configurations | Number of occurrences [%] | Maximum time coverage [%] |
|---|---|---|---|
| 1 | 20 | 17.7 | 33.7 |
| | 26 | 14.5 | 69.4 |
| | 12 | 13.8 | 59.9 |
| 2 | 20, 26 | 16.0 | 72.7 |
| | 26, 28 | 4.7 | 72.4 |
| | 20, 25 | 3.7 | 63.6 |
| 3 | 20, 26, 3 | 9.9 | 87.5 |
| | 20, 26, 28 | 3.5 | 75.6 |
| | 20, 26, 22 | 2.1 | 78.3 |
| 4 | 3, 20, 26, 28 | 4.5 | 88.1 |
| | 1, 3, 20, 26 | 3.8 | 87.5 |
| | 3, 20, 25, 26 | 2.2 | 88.5 |
| 5 | 1, 3, 20, 26, 28 | 3.0 | 88.1 |
| | 1, 3, 20, 25, 26 | 2.5 | 88.5 |
| | 1, 2, 3, 20, 26 | 1.8 | 87.5 |
| 6 | 1, 2, 3, 20, 26, 28 | 3.3 | 88.1 |
| | 1, 2, 3, 20, 25, 28 | 3.2 | 88.5 |
| | 1, 2, 3, 4, 20, 26 | 2.2 | 87.5 |
| 7 | 1, 2, 3, 4, 20, 25, 26 | 3.1 | 88.5 |
| | 1, 2, 3, 4, 20, 26, 28 | 2.8 | 88.1 |
| | 1, 2, 3, 4, 5, 20, 26 | 2.1 | 87.5 |
| 8 | 1, 2, 3, 4, 5, 20, 25, 26 | 3.3 | 88.5 |
| | 1, 2, 3, 4, 5, 6, 20, 26 | 2.1 | 87.5 |
| | 1, 2, 3, 4, 20, 22, 25, 26 | 1.9 | 90.8 |
| 9 | 1, 2, 3, 4, 5, 6, 20, 25, 26 | 3.5 | 88.5 |
| | 1, 2, 3, 4, 5, 6, 20, 26, 28 | 3.4 | 88.1 |
| | 1, 2, 3, 4, 5, 6, 7, 20, 26 | 2.1 | 87.5 |
| 10 | 1, 2, 3, 4, 5, 6, 7, 20, 25, 26 | 3.5 | 88.5 |
| | 1, 2, 3, 4, 5, 6, 7, 8, 20, 26 | 2.3 | 88.1 |
| | 1, 2, 3, 4, 5, 6, 20, 22, 25, 26 | 2.0 | 87.5 |

that different constellations may exhibit varying observational effectivenesses – where one constellation might track an individual fragment for an extended period while another may observe a greater number of fragments but with shorter observation times – two key evaluation metrics are considered. The first metric prioritizes the constellation capable of maximizing the number of fragments monitored for their respective longest durations, and is addresses as occurrences metric. The second prioritizes the one capable of achieving the longest visibility time coverage overall, regardless the number of fragments detected, and is referred as time coverage metrics. The latter metric is deemed the most relevant for maintaining a comprehensive debris catalogue.

*4.3.1. Occurrences metric*

The primary performance parameter evaluated pertains to the optimal occurrences of the constellation. In this context, occurrences is defined as the percentage of fragments for which a specific observer combination is identified as optimal. For a given fragment, a combination is considered optimal if it enables the longest monitoring duration for that specific fragment, compared to all other configurations. To this end, for each number $n$ of observers in the constellation, the three highest-performing combinations, identified as optimal based on the largest number of detectable fragments, are presented in Table 5. The table also reports the corresponding percentage of fragments for which these combinations offer the longest coverage, relative to the total number of fragments generated by collision 7, as well as the maximum visibility time achieved by each combination. The maximum visibility time is defined as the percentage of time instances over a three-month period during which the fragment is detectable by the specific combination of observers.

The results show that the most effective constellation consistently includes the previously identified top-performing observers (see Section 4.2). These key observers – 20, 25, 26 and 12 – correspond to the smallest L2 Lyapunov orbit, the largest L2 Southern Halo orbit, the median L2 Southern Halo orbit, and the smallest L1 Lyapunov orbit, respectively. Observer 20 achieves a maximum coverage time of 33.7% for a given fragment; however, it optimally monitors only 17.7% of fragments. This finding highlights the inherent limitations of single-observer configurations, which fail to provide comprehensive cloud coverage and significantly constrain monitoring duration. Additionally, observer 3 demonstrates strong performance, appearing in all constellation configurations containing between four and ten observers. This finding is not surprising given observer 3 high individual performance, but it is also particularly relevant in the context of the upcoming LUMOS mission [30], as it further supports the potential of this candidate to detect, track, and monitor objects in the Cislunar region.

Expanding the number of observers significantly enhances constellation performance: with a single observer, the highest-performing configuration (observer 20) achieves a coverage time of 33.7%. When three observers are included (3, 20, 26), the best-performing combination reaches 87.5% coverage. By incorporating a fourth observer (3, 20, 26, 28), coverage increases to 88.1%. Notably, the highest recorded coverage time – 90.8% – is achieved with an eight-observer configuration (1, 2, 3, 4, 20, 22, 25, 26). This optimal combination consists of the top-performing observers, reinforcing the conclusion that the most effective constellations primarily rely on these high-performing orbits, while additional observers provide only a minor improvements. Furthermore, when accounting for the maximum time coverage, the

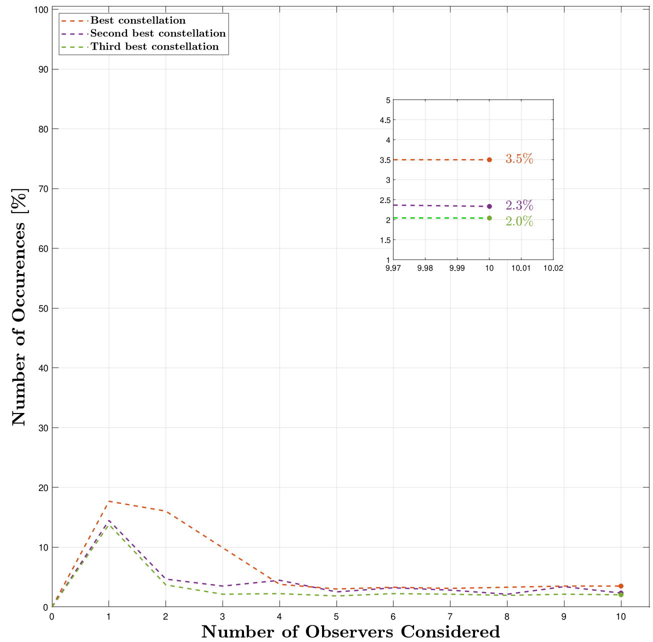


**Fig. 14.** Occurrences Metric: evolution of the percentage of fragments generated by collison 7, for which the three top-performing observers combinations are identified as optimal, in function of the number of observers considered in the constellation. For a given fragment, a combination is considered optimal if it enables the longest monitoring duration for that specific fragment, compared to all other configurations.

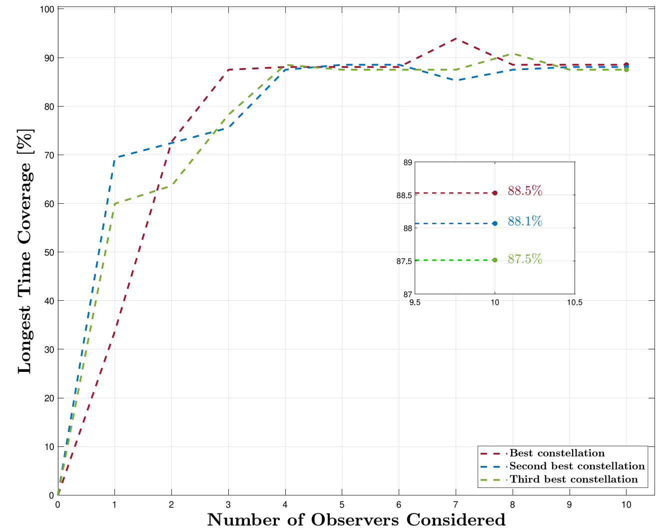


**Fig. 15.** Occurrences Metric: evolution of the maximum percentage of time instances within a three-month period during which the three top-performing combination of observers detects a fragment from collision 7, in function of the number of observers considered in the constellation. The three top-performing combinations are defined through the occurrences metric.

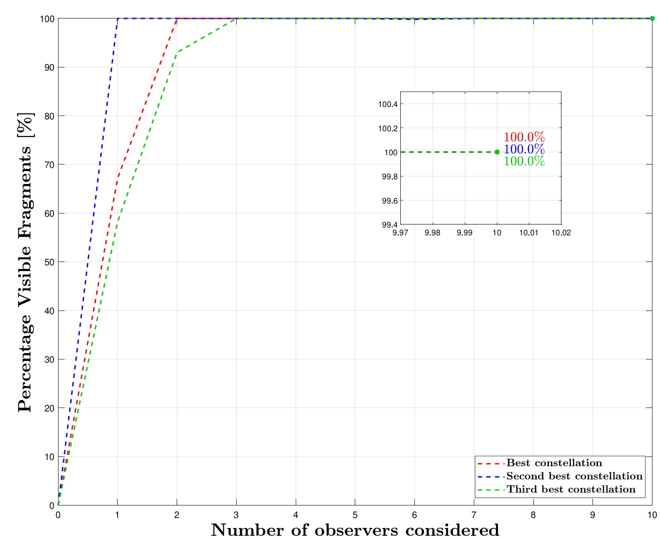


**Fig. 16.** Occurrences Metric: evolution of the percentage of fragments generated by collision 7 that are visible at least once by the three top-performing constellations, as a function of the number of observers considered in the constellation. The three top-performing combinations are defined through the occurrences metric.

peak performance is achieved with an eight-observer configuration. No significant improvements can be observed when increasing the configuration beyond the four-observer setup, thereby making larger configurations both unnecessary and resource-intensive, as no further enhancements in time coverage are attained for this metric.

It is important to note that an increasing number of observers does not directly correspond to a higher percentage of optimally monitored fragments. as highlighted by the comparison of Figs. 14 and 15. In fact, the opposite trend is observed: individual observers tend to track a larger percentage of fragments for their longest recorded duration. However, as the constellation expands, this percentage decreases due to the growing number of possible combinations, which can provide more effective monitoring for specific fragments. For instance, with four observers, the (3, 20, 25, 26) combination achieves the longest coverage of 88.5% but optimally tracks only 3.8% of fragments. In contrast, the combination (3, 20, 26, 28) provides slightly lower overall coverage (88.1%) but has a higher occurrences percentage of 4.5%, meaning it optimally monitors a larger proportion of fragments. As the constellation grows, the percentage of occurrences decreases because more observer combinations are being considered, according to the formula $\binom{29}{n}$. This leads to a higher chance that fragments are monitored more effectively by different configurations. Essentially, while some combinations provide better overall coverage, fewer fragments depend on them as their best option. In contrast, other combinations, although slightly less effective for continuous monitoring, can still play a crucial role in monitoring a larger number of fragments. This insight emphasizes the challenges of optimizing a constellation to both achieve coverage efficiency and monitor a broader range of debris for longer periods. Nevertheless, increasing the number of observers allow all three constellations to eventually detect every fragment at least once, as depicted in Fig. 16.

#### 4.3.2. *Time coverage metric*

The second metric prioritizes the constellation providing the longest visibility coverage time in percentage over three months, across all fragments. According to this metric and as highlighted in Table 6, individual observers 26, 25 and 3 exhibit the highest performance, achieving 69.4%, 63.6%, and 60.9% visibility coverage times, respectively, further validating the suitability of L2 Halo Orbits and DROs for SSA surveillance.

The addition of another spacecraft leads to a noticeable improvement in performance, as illustrated by the matrix of pairwise combinations in Fig. 17. This remains true when increasing the constellation, as highlighted in Table 6 and Fig. 18.

Although the optimal observer combinations change as the number of participants increases, observers 3, 24, 25, 26, 12, 21, 24 and 29 always appear in the highest-performing configurations. These findings suggest that L2 Halo orbits (observers 24, 25, 26) and DRO (observer 3) are ideally suited for monitoring collisions in the L1 Southern Halo, the

**Table 6**
Time coverage metric: the three top-performing constellation combinations are presented as a function of the number of observers considered. The second column presents the maximum visibility time achieved by each combination, defined as the maximum percentage of time instances within a three-month period during which the combination of observers detects a fragment from collision 7.

| n | Three top-performing observers configurations | Maximum time coverage [%] |
|---|---|---|
| 1 | 26 | 69.4 |
| | 25 | 63.6 |
| | 3 | 60.9 |
| 2 | 12, 29 | 87.2 |
| | 3, 24 | 86.6 |
| | 3, 26 | 85.4 |
| 3 | 3, 24, 25 | 92.4 |
| | 12, 21, 29 | 92.2 |
| | 12, 18, 29 | 91.9 |
| 4 | 3, 22, 24, 26 | 94.7 |
| | 8, 12, 21, 29 | 94.6 |
| | 3, 14, 24, 25 | 94.4 |
| 5 | 6, 8, 12, 21, 29 | 96.4 |
| | 6, 8, 12, 18, 29 | 96.0 |
| | 3, 16, 22, 24, 25 | 95.7 |
| 6 | 6, 8, 12, 21, 27, 29 | 97.1 |
| | 6, 8, 12, 21, 23, 29 | 96.9 |
| | 6, 8, 12, 17, 21, 29 | 96.8 |
| 7 | 6, 8, 12, 21, 26, 27, 29 | 97.1 |
| | 6, 8, 12, 21, 26, 23, 29 | 96.9 |
| | 3, 6, 8, 12, 17, 21, 29 | 96.8 |
| 8 | 3, 6, 8, 12, 21, 26, 27, 29 | 97.1 |
| | 3, 6, 8, 12, 21, 23, 26, 29 | 96.9 |
| | 3, 6, 8, 11, 12, 26, 27, 29 | 96.8 |
| 9 | 3, 6, 8, 12, 20, 21, 26, 27, 29 | 97.1 |
| | 3, 6, 8, 12, 20, 21, 23, 26, 29 | 96.9 |
| | 3, 6, 8, 11, 12, 24, 26, 27, 29 | 96.8 |
| 10 | 3, 6, 8, 12, 20, 21, 24, 26, 27, 29 | 97.1 |
| | 3, 6, 8, 12, 20, 21, 23, 24, 26, 29 | 96.9 |
| | 3, 6, 8, 11, 12, 20, 24, 26, 27, 29 | 96.8 |

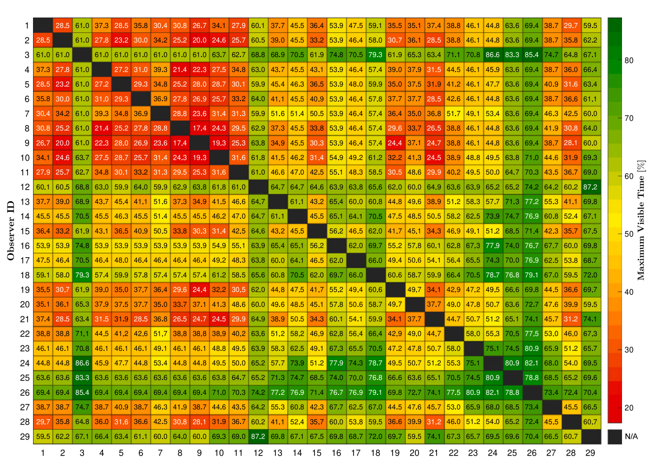


**Fig. 17.** Time Coverage metric: maximum percentage of time instances within a three-month period during which the two-observers combinations detect a fragment from collision 7. The matrix is symmetric and the main diagonal reports a not-applicable percentage, as a sensor cannot be combined with itself.

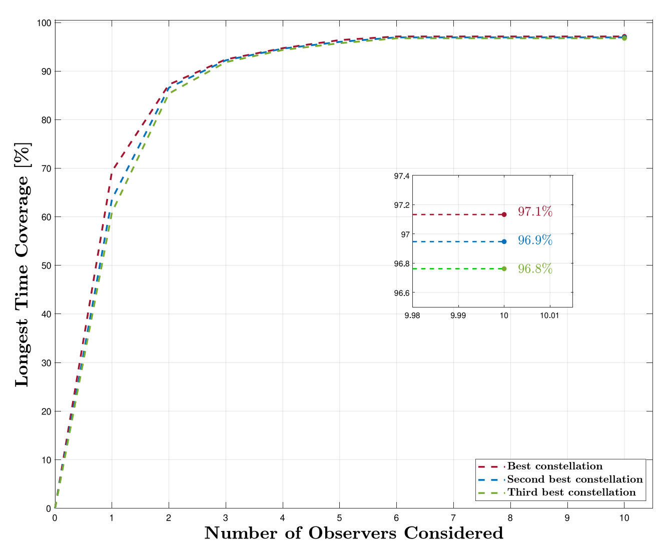


**Fig. 18.** Time Coverage metric: evolution of the maximum percentage of time instances within a three-month period during which the three top-performing combination of observers detects a fragment from collision 7, in function of the number of observers considered in the constellation.

orbital regime where the analyzed collision 7 is located. Additionally, the performance of these orbits could be further enhanced by incorporating L1 Lyapunov orbits (observer 12), L2 Lyapunov orbits (observers 20, 21), and ELOs (Observer 29). This last result is quite interesting, as deploying observers on lunar orbits would not only enable detailed monitoring of that orbital regime, but also provide coverage of the Cislunar region when integrated into a constellation. Interestingly, the top-performing observers identified in the single-observer analysis remain the best candidates within larger constellations, reconfirming that certain observers consistently offer optimal coverage, with additional observers filling the visibility gaps.

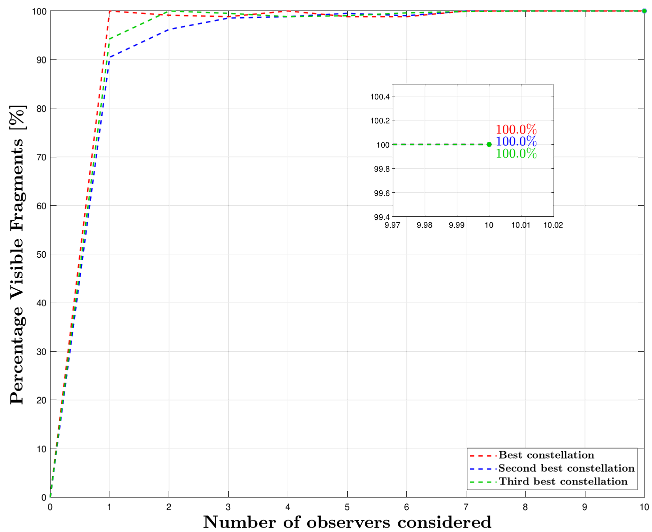


**Fig. 19.** Time Coverage Metric: evolution of the percentage of fragments generated by collision 7 that are visible at least once by the three top-performing constellations, as a function of the number of observers considered in the constellation.

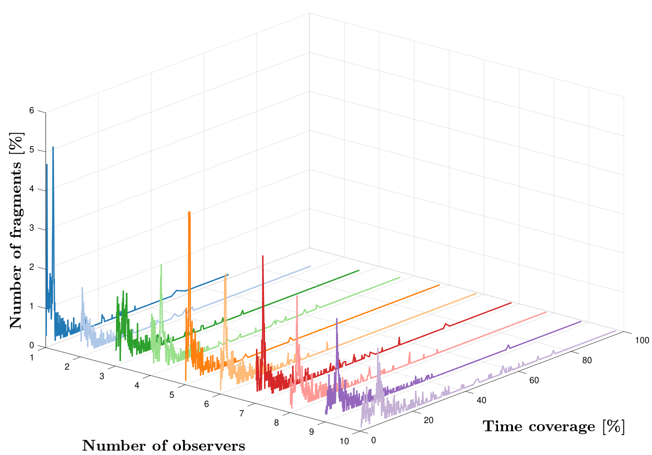


**Fig. 20.** Time Coverage Metric: correlation of the percentage of fragments generated by collision 7, visible by the top-performing constellation and the respective maximum visibility time, expressed in days, as a function of the number of observers considered in the constellation. The three top-performing combinations are defined through the time coverage metric.

As the number of observers increases, coverage surpasses 97% when six observers are considered. However, from n = 6 onward, performance stabilizes, yielding diminishing returns with further additions. The optimal performance is therefore achieved with six observers and beyond this point further increases in the constellation size provide minimal benefits in terms of coverage.

Similarly to Section 4.3.1 and highlighted in Fig. 19, expanding the constellation may facilitate the detection of a greater number of fragments at least once. Moreover, this outcome remains strongly dependent on the presence of high-performing observers. This effect is particularly evident in the 'best performance' trend where 100% fragment detection is achieved at n = 1, n = 4, and from n = 7 onward, coinciding with the reintroduction of observer 26. Thus, the expansion of the constellation should be carefully balanced against available resources and mission objectives. Additionally, the strategic placement of observers remains critical to maximizing both the effectiveness and overall efficiency of the constellation.

To complete the analysis, Fig. 20 illustrates the distribution of fragments versus the total covered time in days, in the function of the number of observers considered in the constellation for the top-performing constellation. As the number of observers increases, the maximum coverage time improves, reaching 87.4 days with six observers. However, the longest coverage durations are associated with individual fragments, while the majority are tracked for relatively short periods, as indicated by the initial peaks on the time-coverage axis in Fig. 20. Despite this trend, constellation expansion improves the capability to monitor a greater number of fragments for longer durations, even if the maximum coverage times are not reached. Notably, the peaks observed at the beginning of the period of observation exhibit a tendency to flatten, suggesting that a larger constellation can offer significant operational advantages by monitoring a greater percentage of fragments for longer periods.

## 5. Conclusions

This study provides a comprehensive analysis of debris evolution and detectability within the Cislunar environment, offering critical insights into the complexities of this region and contributing to the requirements for a space-based STM infrastructure, capable of enabling the sustainable long-term utilization of Cislunar space.

Nine families of periodic orbits are selected for potential Cislunar observation: DRO, L4 Planar, L5 Planar, L1 Lyapunov, L1 Northern Halo, L1 Southern Halo, L2 Lyapunov, L2 Northern Halo, and L2 Southern Halo. A total of eleven collision scenarios are simulated across the orbits within these families and twenty-eight observers deployed. A further space-based observer is placed on a relevant ELO for a total of twenty-nine observers.

Moderate risks of impacts with celestial bodies, particularly the Moon, are identified. In contrast, minimal risks are associated with the GEO belt region, as the majority of debris intersecting this region, do so at nearly normal angles.

Over a three-month period, the majority of debris fragments disperse chaotically across the Cislunar region. However, lower-velocity fragments tend to concentrate in the inner Cislunar zone, enabling prolonged detectability, particularly around the more stable L2 Halo orbits, which is proven highly effective for the deployment of a space-based observer for cataloguing space debris generated by fragmentations in the Cislunar region. In contrast, fragments with large velocity disperse across the region, ultimately making the fragments undetectable due to the significant distances involved.

The L2 Halo and Lyapunov orbits, followed by smaller DROs and L1 Lyapunov orbits, emerged as the most effective orbital families for debris monitoring, establishing them as promising candidates for hosting an STM infrastructure. Furthermore, at a space mission design phase, satellite positioning can be based on considerations regarding potential fragmentation. For instance, the monitoring of the breakup of a satellite placed in the Southern L1 Halo orbit would benefit from more effective observation when supported by space-based sensors positioned in L2 orbits. This strategic alignment could inform debris mitigation strategies.

The tracking of the fragments generated by a collision occurred in Cislunar region significantly improves when multiple observer satellites operate in a constellation. Increasing the number of observers enhances the time coverage of a single fragment on a three-month time window, achieving up to 97.1% of visibility time with a six-observers constellation. However, beyond six observers, further resource allocation yields diminishing returns. To analyze this behavior and evaluate how increasing the size of the observers constellation may enhance performance, two metrics are considered: one that prioritizes the maximum percentage of fragments for which a combination provides its relative longest visibility time, and another that prioritizes the overall longest visibility time. For both metrics analyzed, a small number of highly efficient observers, primarily located in L2 Halo orbits, consistently form the most effective debris-detecting constellations. The performance of these constellations can be further optimized by incorporating L1 Lyapunov orbits, small DROs, or lunar orbits such as ELOs, effectively complementing the L2 Halo orbits. Given their critical role in both the development of surveillance constellations and the advancement of scientific research, the L2 Halo regions are expected to experience the highest concentration of operational assets. As such, careful planning and design for the utilization of these regions are recommended to minimize the potential for fragmentation events and to ensure the safety of future operations.

These findings extend beyond current literature on Cislunar fragmentation event analysis, mainly based on explosions test cases [4–7,46] and provide key insights for the development of an advanced, tailored STM infrastructure, playing a critical role in supporting the sustainable utilization of this pivotal region.

Several potential developments of this work are possible and outlined hereafter. First, the modeling and analysis of debris trajectories in Cislunar space could be enhanced by employing higher-fidelity methods, such as the Bicircular Restricted Four-Body Problem [25] or the Ephemeris-based N-body model [4]. Additionally, sensitivity analyses could be conducted by varying key fragmentation factors, such as the type of breakup, the involved spacecraft, the breakup epoch, and the impact velocity, to examine how these variations influence debris cloud trajectories and their observability. Improving observability could also be achieved by deploying additional satellites along the optimal orbits or using advanced observability models [18,21], which could refine sensor measurement simulations. Finally, the integration of alternative breakup models, including semi-empirical models like FAST [47] or IMPACT [48] and more advanced tools such as the Collision Simulation Tool [49] or the CARDC-SBM spacecraft breakup model [50], could provide more realistic simulations of collision dynamics and offer valuable insights into debris distribution.

## CRediT authorship contribution statement

**C. Gambarotto:** Writing – review & editing, Writing – original draft, Visualization, Validation, Software, Methodology, Investigation, Formal analysis, Data curation, Conceptualization. **P. Grattagliano:** Writing – review & editing, Visualization, Supervision, Software, Resources, Methodology, Investigation, Formal analysis, Conceptualization. **L. De Maria:** Writing – review & editing, Visualization, Supervision, Resources, Methodology, Formal analysis, Data curation, Conceptualization. **M.F. Montaruli:** Writing – review & editing, Supervision, Resources, Project administration, Methodology, Funding acquisition, Formal analysis, Conceptualization.

## Declaration of competing interest

The authors declare that they have no known competing financial interests or personal relationships that could have appeared to influence the work reported in this paper.

## Appendix. Conversion from inertial J2000 to synodic reference frame

For practical applications, it is often advantageous to express trajectories in the J2000 reference frame, which is inertial and Earth-centered. In this frame, the x-axis points towards the Vernal equinox at epoch J2000 (that is, at 12:00 Terrestrial Time on January 1st, 2000), the z-axis is aligned with the Earth's rotation axis, and the y-axis is orthogonal to both the x- and z-axes, completing the right-handed coordinate system [51].

To achieve this, the transformation from the inertial J2000 reference frame (denoted as J) to the Synodic reference frame (denoted as S) is performed as follows [52].

For a given epoch $t$, the J2000 position and velocity vectors are transformed into an instantaneous rotating frame, which is defined in terms of unit vectors relative to the J2000 frame and identified as Synodic Earth-Centered reference frame (SEC):

$$\begin{bmatrix}\mathbf{r}(t)\\ \mathbf{v}(t)\end{bmatrix}_{SEC} = \begin{bmatrix}\mathbf{C} & \mathbf{0}_{3\times3}\\ \dot{\mathbf{C}} & \mathbf{C}\end{bmatrix}^{-1} \begin{bmatrix}\mathbf{r}(t)\\ \mathbf{v}(t)\end{bmatrix}_{J} \tag{9}$$

where $\mathbf{C}$ is the transformation matrix, and $\dot{\mathbf{C}}$ its time derivative, defined as:

$$\mathbf{C} = \begin{bmatrix}\mathbf{X}_{ref} & \mathbf{Y}_{ref} & \mathbf{Z}_{ref}\end{bmatrix} \tag{10}$$

$$\dot{\mathbf{C}} = \begin{bmatrix}\dot{\theta}C_{12} & -\dot{\theta}C_{11} & 0\\ \dot{\theta}C_{22} & -\dot{\theta}C_{21} & 0\\ \dot{\theta}C_{32} & -\dot{\theta}C_{31} & 0\end{bmatrix} \tag{11}$$

The elements $C_{ij}$ are the matrix $\mathbf{C}$ components and the unit vectors defining the reference frame are given by:

$$\mathbf{C} = \begin{cases}\mathbf{X}_{ref} = & \frac{\mathbf{R}_{Moon}}{\|\mathbf{R}_{Moon}\|}\\ \mathbf{Z}_{ref} = & \frac{\mathbf{R}_{Moon}\times\dot{\mathbf{R}}_{Moon}}{\|\mathbf{R}_{Moon}\times\dot{\mathbf{R}}_{Moon}\|}\\ \mathbf{Y}_{ref} = & \mathbf{Z}_{ref}\times\mathbf{X}_{ref}\end{cases} \tag{12}$$

The angular velocity $\dot{\theta}$ is defined as:

$$\dot{\theta} = \frac{\mathbf{R}_{Moon}\times\dot{\mathbf{R}}_{Moon}}{\|\mathbf{R}_{Moon}\|^2} \tag{13}$$

where $\mathbf{R}_{Moon}$ is the Moon position vector in the J2000 inertial coordinates at epoch $t$, and $\dot{\mathbf{R}}_{Moon}$ is its velocity vector.

Subsequently, the origin of the Synodic reference frame is shifted from the Earth to the Earth-Moon system barycenter and the parameters are adimensionalized:

$$\mathbf{r}_S(t) = \mathbf{r}_{SEC}(t)\ \frac{1}{l^*} - \begin{bmatrix}\mu\\ 0\\ 0\end{bmatrix} \tag{14}$$

$$\mathbf{v}_S(t) = \mathbf{v}_{SEC}(t)\ \frac{\tau}{l^*} \tag{15}$$

$$t_S = \frac{t_J}{\tau} \tag{16}$$

where

$$\mu = \mu_{Earth} + \mu_{Moon} \tag{17}$$

$$l^* = \|\mathbf{R}_{\mathbf{Moon}}\| \tag{18}$$

$$\tau = \sqrt{\frac{(l^*)^3}{\mu}} \tag{19}$$

In this formulation, $l^*$ represents the Earth-Moon distance, and $\mu_{sum}$ is the total gravitational parameter of the Earth-Moon system. The time scale $\tau$ is defined as the standard gravitational time constant for the system.

The inverse transformation can be applied to convert the state from the Synodic reference frame back to the J2000 reference frame.

## References

[1] K. Johnson, Fly me to the moon: Worldwide Cislunar and Lunar missions, 2022.
[2] M.J. Holzinger, C.C. Chow, P. Garretson, A primer on cislunar space, 2021.
[3] D.E. Lee, White paper: Gateway destination orbit model: A continuous 15 year nrho reference trajectory, 2019.
[4] P. Guardabasso, D.K. Skoulidou, L. Bucci, F. Letizia, S. Lemmens, M. Ansart, X. Roser, S. Lizy-Destrez, G. Casalis, Analysis of accidental spacecraft break-up events in cislunar space, Adv. Space Res. 72 (5) (2023) 1550–1569.
[5] A. Black, C. Frueh, Characterizing cislunar fragmentations, in: Proceedings of the Advanced Maui Optical and Space Surveillance (AMOS) Technologies Conference, 2023, p. 20.
[6] N.R. Boone, R.A. Bettinger, Debris collision risk analysis following simulated cislunar spacecraft explosions, J. Spacecr. Rockets 60 (2) (2023) 668–684.

[7] N.R. Boone, Cislunar Debris Propagation Following a Catastrophic Spacecraft Mishap Master's thesis, Air Force Institute of Technology, Wright-Patterson Air Force Base, Ohio, 2021, URL https://scholar.afit.edu/etd/4971.

[8] E.E. Fowler, S.B. Hurtt, D.A. Paley, Orbit design for cislunar space domain awareness, in: 2nd IAA Conference on Space Situational Awareness, ICSSA, Washington, District of Columbia, 2020.

[9] E. SST, EU space surveillance & tracking: Service portfolio. 2024, 2024.

[10] T. Flohrer, H. Krag, Space surveillance and tracking in esa's SSA programme, in: Proceedings 7th European Conference on Space Debris, Vol. 1, Darmstadt, Germany, 2017, https://Conference.Sdo.Esoc.Esa.Int.

[11] M.F. Montaruli, P. Di Lizia, E. Cordelli, H. Ma, J. Siminski, A stochastic approach to detect fragmentation epoch from a single fragment orbit determination, Adv. Space Res. 72 (2023) http://dx.doi.org/10.1016/j.asr.2023.08.031.

[12] S. Bonaccorsi, M.F. Montaruli, P. Di Lizia, M. Peroni, A. Panico, M. Rigamonti, F. Del Prete, Conjunction analysis software suite for space surveillance and tracking, Aerospace (ISSN: 2226-4310) 11 (2) (2024) http://dx.doi.org/10.3390/aerospace11020122, URL https://www.mdpi.com/2226-4310/11/2/122.

[13] A. Muciaccia, L. Facchini, M.F. Montaruli, G. Purpura, R. Detomaso, C. Colombo, M. Massari, P. Di Lizia, A. di Cecco, L. Salotti, G. Bianchi, Radar observation and recontruction of cosmos 1408 fragmentation, J. Space Saf. Eng. 11 (2023) http://dx.doi.org/10.1016/j.jsse.2023.11.006.

[14] M.F. Montaruli, G. Purpura, R. Cipollone, A.D. Vittori, L. Facchini, P. Di Lizia, M. Massari, M. Peroni, A. Panico, A. Cecchini, M. Rigamonti, An orbit determination software suite for space surveillance and tracking applications, CEAS Space J. (ISSN: 1868-2510) 16 (5) (2024) 619–633, http://dx.doi.org/10.1007/s12567-024-00535-1.

[15] M.F. Montaruli, P. Di Lizia, S. Tebaldini, G. Bianchi, Adaptive track approach for multiple sources scenarios during radar survey for space surveillance applications, Aerosp. Sci. Technol. (ISSN: 1270-9638) 152 (2024) 109307, http://dx.doi.org/10.1016/j.ast.2024.109307, URL https://www.sciencedirect.com/science/article/pii/S1270963824004383.

[16] M.F. Montaruli, M.A. De Luca, M. Massari, G. Bianchi, A. Magro, Operational angular track reconstruction in space surveillance radars through an adaptive beamforming approach, Aerospace (ISSN: 2226-4310) 11 (6) (2024) http://dx.doi.org/10.3390/aerospace11060451, URL https://www.mdpi.com/2226-4310/11/6/451.

[17] M.F. Montaruli, L. Facchini, P. Di Lizia, M. Massari, G. Pupillo, G. Bianchi, G. Naldi, Adaptive track estimation on a radar array system for space surveillance, Acta Astronaut. (ISSN: 0094-5765) 198 (2022) 111–123, http://dx.doi.org/10.1016/j.actaastro.2022.05.051, URL https://www.sciencedirect.com/science/article/pii/S0094576522002703.

[18] E.E. Fowler, D.A. Paley, Observability metrics for space-based cislunar domain awareness, J. Astronaut. Sci. 70 (2) (2023) 10.

[19] C. Frueh, K. Howell, K.J. DeMars, S. Bhadauria, Cislunar space situational awareness, in: 31st AIAA/AAS Space Flight Mechanics Meeting, 2021, pp. 6–7.

[20] M.R. Thompson, N.P. Ré, C. Meek, B. Cheetham, Cislunar orbit determination and tracking via simulated space-based measurements, in: Advanced Maui Optical and Space Surveillance Technologies Conference, Maui, HI, 2021.

[21] J.K. Vendl, M.J. Holzinger, Cislunar periodic orbit analysis for persistent space object detection capability, J. Spacecr. Rockets 58 (4) (2021) 1174–1185.

[22] B.P. Baker-McEvilly, J. Rose, S. Bhadauria, D. Canales, C. Frueh, H. Cho, Performance of observational spacecraft across orbit families for space domain awareness in the cislunar realm, in: AIAA SCITECH 2024 Forum, 2024, p. 2067.

[23] A.P. Wilmer, R.A. Bettinger, B.D. Little, Cislunar periodic orbits for earth–moon L1 and L2 Lagrange point surveillance, J. Spacecr. Rockets 59 (6) (2022) 1809–1820.

[24] A.P. Wilmer, R.A. Bettinger, Near-rectilinear halo orbit surveillance using cislunar periodic orbits, in: 2022 Advanced Maui Optical and Space Surveillance Technologies Conference, AMOS, 2022.

[25] A.P. Wilmer, R.A. Bettinger, B.D. Little, Preliminary viability assessment of cislunar periodic orbits for space domain awareness, in: 2021 Advanced Maui Optical and Space Surveillance Technologies Conference, AMOS, 2021.

[26] T.H. Clareson, M.C. Fox, D.K. Amato, H.W. Lee, Embedded state estimation for optimization of cislunar space domain awareness constellation design, J. Spacecr. Rockets 62 (3) (2025) 898–914.

[27] M. Patel, Y. Shimane, H.W. Lee, K. Ho, Cislunar satellite constellation design via integer linear programming, J. Astronaut. Sci. 71 (3) (2024) 26.

[28] J.M. Block, D.H. Curtis, R.A. Bettinger, A.P. Wilmer, Cislunar SDA with low-fidelity sensors and observer uncertainty, Sat 1000 (2022) 1.

[29] J.S. Parker, R.L. Anderson, Low-Energy Lunar Trajectory Design, Vol. 12, John Wiley & Sons, 2014.

[30] E.S. Agency, Studies/reviews, 2024, URL https://www.esa.int/Enabling_Support/Space_Engineering_Technology/CDF/Studies_Reviews, (Accessed 02 November 2024).

[31] T. Ely, Stable constellations of frozen elliptical inclined lunar orbits, J. Astronaut. Sci. 53 (3) (2005) 301–316.

[32] Z.-Y. Gao, X.-Y. Hou, Coverage analysis of lunar communication/navigation constellations based on halo orbits and distant retrograde orbits, J. Navig. 73 (4) (2020) 932–952.

[33] R. Whitley, R. Martinez, Options for staging orbits in cislunar space, in: 2016 IEEE Aerospace Conference, IEEE, 2016, pp. 1–9.

[34] A.F.R. Laboratory, Cislunar Highway Patrol System, Air Force Research Laboratory, 2022.

[35] R.M. Greenwich, NASA moon mission: Artemis program launch date, 2024, URL https://www.rmg.co.uk/stories/topics/nasa-moon-mission-artemis-program-launch-date, (Accessed 21 August 2024).

[36] C. Li, W. Zuo, W. Wen, X. Zeng, X. Gao, Y. Liu, Q. Fu, Z. Zhang, Y. Su, X. Ren, et al., Overview of the Chang'e-4 mission: Opening the frontier of scientific exploration of the lunar far side, Space Sci. Rev. 217 (2021) 1–32.

[37] N.L. Johnson, P.H. Krisko, J.-C. Liou, P.D. Anz-Meador, NASA's new breakup model of EVOLVE 4.0, Adv. Space Res. 28 (9) (2001) 1377–1384.

[38] J. Schuhmacher, Efficient Implementation and Evaluation of the NASA Breakup Model in Modern C++, Technische Universität München, 2021.

[39] LivingFuture, LivingFuture.cz - home page, 2024, https://www.livingfuture.cz/index_en.php, (Accessed 16 April 2024).

[40] E.S.A. (ESA), Lunar missions overview, 2019, https://www.esa.int/ESA_Multimedia/Images/2019/07/Lunar_missions_overview, (Accessed 16 April 2024).

[41] T. Gardner, B. Cheetham, A. Forsman, C. Meek, E. Kayser, J. Parker, M. Thompson, T. Latchu, R. Rogers, B. Bryant, et al., Capstone: A cubesat pathfinder for the lunar gateway ecosystem, 2021.

[42] F. Topputo, G. Merisio, V. Franzese, C. Giordano, M. Massari, G. Pilato, D. Labate, A. Cervone, S. Speretta, A. Menicucci, et al., Meteoroids detection with the LUMIO lunar CubeSat, Icarus 389 (2023) 115213.

[43] E.S.A. (ESA), Space safety industry day 2024, 2024, https://indico.esa.int/event/544/attachments/6448/11369/Space%20Safey%20Industry%20Day%202024.pdf, (Accessed 16 April 2024).

[44] NASA Jet Propulsion Laboratory, NAIF toolkit, 2023, URL https://naif.jpl.nasa.gov/naif/toolkit.html, (Accessed 10 October 2024).

[45] J. Slíz-Balogh, A. Barta, G. Horváth, Celestial mechanics and polarization optics of the Kordylewski dust cloud in the Earth–Moon Lagrange point L5–Part II. Imaging polarimetric observation: new evidence for the existence of Kordylewski dust cloud, Mon. Not. R. Astron. Soc. 482 (1) (2019) 762–770.

[46] A. Wilmer, N. Boone, R. Bettinger, Artificial debris propagation in cislunar periodic orbits, in: 2021 Astrodynamics Specialist Conference, AAS Paper, 2021, pp. 21–525.

[47] D. McKnight, R. Maher, L. Nagl, Fragmentation algorithms for strategic and theater targets (FASTT) empirical breakup model, 1994, DNA-Kaman, January.

[48] D.L. Mains, M.E. Sorge, The IMPACT satellite fragmentation model, Acta Astronaut. 195 (2022) 547–555.

[49] A. Francesconi, C. Giacomuzzo, L. Olivieri, G. Sarego, M. Duzzi, F. Feltrin, A. Valmorbida, K.D. Bunte, M. Deshmukh, E. Farahvashi, et al., CST: A new semi-empirical tool for simulating spacecraft collisions in orbit, Acta Astronaut. 160 (2019) 195–205.

[50] T. Yao, Z. Yang, Y. Luo, S. Lan, L. Ren, Generation of initial debris cloud distributions for breakup events based on CARDC-SBM, Acta Astronaut. 219 (2024) 580–591.

[51] N. Navigation, A.I.F. (NAIF), Frames and coordinate systems, 2022, URL https://naif.jpl.nasa.gov/pub/naif/toolkit_docs/Tutorials/pdf/individual_docs/17_frames_and_coordinate_systems.pdf, (Accessed 12 November 2024).

[52] T.A. Pavlak, Trajectory Design and Orbit Maintenance Strategies in Multi-Body Dynamical Regimes (Ph.D. thesis), Purdue University, 2013.